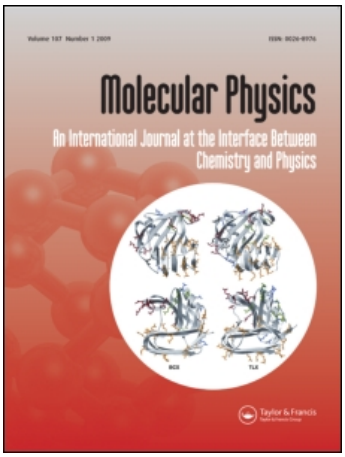

Molecular Physics
Publication details, including instructions for authors and subscription information:
http://www.informaworld.com/smpp/title~content=t713395160

Jahn-Teller distortions in the electronically excited states of sym-triazine

V. A. Mozhayskiy [a]; A. I. Krylov [a]
[a] Department of Chemistry, University of Southern California, Los Angeles, CA 90089-0482, USA

First Published:January2009

To cite this Article Mozhayskiy, V. A. and Krylov, A. I.(2009)'Jahn-Teller distortions in the electronically excited states of sym-triazine',Molecular Physics,107:8,929 — 938
To link to this Article: DOI: 10.1080/00268970802705732
URL: http://dx.doi.org/10.1080/00268970802705732

Molecular Physics
Vol. 107, Nos. 8–12, 20 April–20 June 2009, 929–938

Taylor & Francis
Taylor & Francis Group

INVITED ARTICLE

Jahn–Teller distortions in the electronically excited states of *sym*-triazine

V.A. Mozhayskiy and A.I. Krylov*

Department of Chemistry, University of Southern California, Los Angeles, CA 90089-0482, USA

(*Received 3 November 2008; final version received 16 December 2008*)

Electronic structure of the low-lying excited states of *sym*-triazine is analysed. Excitation energies are computed at the equilibrium ground state geometry and at the geometry of the cation. Full geometry optimisations of the selected excited states were performed, and the magnitude of the Jahn–Teller distortions in these states was quantified. Analysis of the electronic structure of these states offers a simple recipe for predicting the symmetry of the equilibrium geometries by a single point calculation of the vertical excitations. Whereas the states derived from excitations between a degenerate pair and a non-degenerate orbital form a familiar two-state conical intersection and are always distorted by virtue of the Jahn–Teller theorem, the states derived from the excitations between two pairs of degenerate orbitals form a more complicated glancing-like manifold characterised by negligible Jahn–Teller linear terms. Our analysis shows that regardless of the degeneracy pattern in these four-state manifolds, the top two states are always nearly-symmetric. The particular shape of the potential energy surfaces in a glancing intersection depends on the relative ordering of the states within the manifold, and different topologies of both types of intersections around D_{3h} geometry are discussed. Predicted symmetry of the excited states is compared to the optimised structures of the selected electronic states.

Keywords: conical intersection; glancing intersection; potential energy surfaces; equation-of-motion coupled-cluster methods; *ab initio*; refection principle

1. Introduction

Triazine is the simplest member of the azobenzenes family, and its isomers have attracted considerable experimental and theoretical attention [1–12]. Triazines are isoelectronic with benzene, the simplest aromatic molecule, however, the presence of heteroroatoms introduces an interesting twist in their electronic structure and allows one to investigate how chemical and physical properties of benzene (e.g. aromaticity) are modulated in homologous series.

One important difference between azobenzenes and benzene is their very dense electronic spectra [1]. In addition to the benzene-like ($\pi \longrightarrow \pi^*$ and $\pi \longrightarrow R$) transitions, they include numerous transitions derived from the $n \longrightarrow \pi^*$ and $n \longrightarrow R$ excitations. Owing to the complexity of the electronic spectroscopy of azobenzenes they have become popular benchmark systems for electronic structure methodology [5,8,10,12].

Chemically, azobenzenes are less stable than benzene and, consequently, have a propensity to undergo three-body dissociation. Among the three isomers of triazine, *sym*-triazine (Tz) is of special importance due to its high symmetry and the ability to dissociate into three identical fragments, which motivated a number of experimental and theoretical studies of this system [2,6,7,9,11,13–15]. The central question in these studies was whether the mechanism of the three-body break-up is concerted or stepwise. Recent experiments in Continetti's group, in which HCN fragments were detected in coincidence with time and position resolution [16–18], demonstrated that both dissociation channels are open. While the mechanisms of concerted and stepwise dissociation have not yet been fully elucidated, most researchers agree that dissociation occurs following radiationless transition of electronically excited Tz to the ground electronic state [9,11,13]. Theoretical investigations of the ground state potential energy surface (PES) of Tz have found that the lowest transition state between the Tz molecule and the three HCN products is of D_{3h} symmetry [6,11], thus fulfilling a necessary condition for the concerted symmetric dissociation. The two channels have been explained in terms of different initial conditions using the reflection principle. The symmetric distribution of energy and momentum among the three HCN fragments (concerted dissociation) ensues when the dynamics on the ground state PES is initiated from the symmetric wave packet, whereas asymmetric momentum distribution results from the wave packet with vibrational excitation in the

*Corresponding author. Email: krylov@usc.edu

ISSN 0026–8976 print/ISSN 1362–3028 online

DOI: 10.1080/00268970802705732
http://www.informaworld.com

asymmetric vibrational modes. Using Franck–Condon arguments (and assuming that the excited state lifetimes are sufficiently long such that the vibration wave packet can equilibrate prior to radiationless relaxation to the ground state), a symmetric wave packet can be attributed to the relaxation from the electronic state with a symmetric PES, whereas the transition from an electronic state with an asymmetric (non-D_{3h}) PES will produce a non-symmetric wave packet. Thus, characterising equilibrium geometries of the excited electronic states of Tz played an important role in the theoretical interpretation of Continetti's experiments [16–18].

Due to the high symmetry of Tz (D_{3h}), many of its electronic and ionised states are derived from the transitions involving degenerate molecular orbitals (MOs), and, consequently, many of them are subject to Jahn–Teller (JT) distortions. Whereas the ionised states or states derived from the transitions in which either initial or target MOs are degenerate form a familiar 'Mexican-hat' two-state Jahn–Teller manifold, the states derived from the transitions between the pairs of degenerate MOs from a more complicated four-state manifold, in which the JT distortions of the two exactly degenerate states are so small that their intersection appears to be glancing rather than conical. This type of intersection has been characterised in N_3^+ both formally and computationally [19,20].

The focus of this paper is on characterising the two types of Jahn–Teller intersections in Tz. We further analyse the topologies of these manifolds and present a simple recipe of predicting whether a particular state from the glancing-like manifold has a distorted or nearly symmetric equilibrium structure from only one single point calculation at a symmetric geometry and the analysis of the electronic structure of the excited states. We also present optimised equilibrium geometries for the selected states to validate the predictions of this simple analysis and to quantify the magnitude of the JT distortions. Finally, we analyse the optimised geometries in terms of the displacements along normal modes of the ground-state Tz to make a connection with Conitnetti's experiments [16–18].

2. Theoretical methods and computational details

The ground state equilibrium geometry and vibrational frequencies were computed by the coupled-cluster with single and double substitutions (CCSD) method [21] with the cc-pVTZ basis set [22]. Excitation energies and optimised structures of the electronically excited states were computed by equation-of-motion for excitation energies CCSD (EOM-EE-CCSD) [23–27]. The EOM-EE methods are capable of reproducing electronic degeneracies (e.g. in Jahn–Teller systems), as well as a balanced description of interacting states of different character (e.g. Rydberg and valence), which is crucial in the case of Tz in view of its dense electronic spectrum and multiple JT manifolds. Equilibrium geometries and frequencies of the cation were computed by EOM-CCSD for ionisation potentials (EOM-IP-CCSD) [28–30] and the cc-pVTZ basis set [22]. All geometry optimisations were conducted using analytic nuclear gradients EOM-CCSD and CCSD codes [30,31].

All electrons were correlated in geometry optimisations and excitation energy calculations. All calculations were performed using the Q-CHEM electronic structure program [32].

Basis set effects were investigated using a series of Pople basis sets with a varying number of diffuse and polarisation basis functions [33,34]. Vertical excitation energies of Tz at the CCSD/cc-pVTZ geometry calculated with different bases are summarised in Table 1. Most of the excited states energies of states are almost converged at the 6-311++G** level, e.g. the differences in the excitation energies relative to aug-cc-pVTZ do not exceed 0.05 eV for all the states below 8 eV, except some Rydberg and higher $n \rightarrow \pi^*$ states. For example, adding a second set of diffuse functions lowers excitation energies of the Rydberg states by 0.1 eV on average. Extra polarisation functions increase energies of all the states by about 0.1 eV. Higher $n \rightarrow \pi^*$ states are mixed with a high density manifold of the Rydberg states in this energy region, which results in a stronger basis set dependence of the high valence states of the same symmetry as $n \rightarrow R_p$ states. The differences in excitation energies between the aug-cc-pVTZ basis and a corresponding (but slightly smaller) Pople basis, 6-311(2+,+)G(3df, 3pd), do not exceed 0.08 eV, and for most states are within 0.02 eV. Overall, the 6-311++G** basis set provides a balanced description of the valence states of Tz, and the results for the Rydberg states are close to the aug-cc-pVTZ ones due to the cancellation of errors. Thus, most of the excited states calculations presented below employ this basis set.

3. Electronically excited states at the neutral and the cation geometries: assignments and symmetry analysis

Excitation energies and symmetries of the lowest excited states of Tz at the equilibrium geometries of the neutral and the cation are shown in Figure 1. Both singlet and triplet manifolds are very dense and feature

Table 1. Total ground state energies (Hartrees) and vertical excitation energies (eV) of Tz calculated by EOM-CCSD.

		Basis set				
		6-311(+, +)G**	6-311(2+, +)G**	6-311(+, +)G(3df, 3pd)	6-311(2+, +)G(3df, 3pd)	aug-cc-pVTZ
Ground state						
	HF, Hartree	−278.761264	−278.761497	−278.787863	−278.787902	−278.792627
	CCSD, Hartree	−279.798375	−279.799375	−279.981261	−279.981525	−279.963019
Singlets						
$n\pi^*$	$^1A_1''$	4.99	4.99	4.96	4.96	4.95
	$^1A_2''$	5.04	5.04	5.02	5.02	5.02
	$^1E'$	5.06	5.06	5.03	5.03	5.03
$\pi\pi^*$	$^1A_2'$	6.01	6.01	6.00	6.00	6.00
	$^1A_1'$	7.54	7.53	7.43	7.42	7.42
	$^1E'$	8.43	8.39	8.24	8.19	8.21
$n_{-1}\pi^*$	$^1E''$	8.18	8.01	8.15	8.09	8.14
nR_s	$^1E'$	7.41	7.30	7.53	7.44	7.46
nR_p	$^1A_2'$	8.24	8.13	8.36	8.23	8.30
	$^1E'$	8.25	8.12	8.46	8.43	8.40
	$^1A_1'$	8.29	8.11	8.39	8.26	8.30
Triplets						
$n\pi^*$	$^3A_2''$	4.52	4.52	4.54	4.53	4.54
	$^3E''$	4.71	4.71	4.70	4.70	4.70
	$^3A_1''$	4.99	4.99	4.94	4.94	4.94
$\pi\pi^*$	$^3A_1'$	4.80	4.79	4.82	4.81	4.83
	$^3E'$	5.82	5.82	5.77	5.77	5.78
	$^3A_2'$	6.83	6.83	6.68	6.68	6.67
$n_{-1}\pi^*$	$^3E''$	7.57	7.56	7.54	7.54	7.55
nR_s	$^3E'$	7.34	7.24	7.45	7.37	7.39
nR_p	$^3A_1'$	8.08	7.91	8.20	8.19	8.11
	$^3A_2'$	8.23	8.12	8.35	8.25	8.29
	$^3E'$	8.26	8.11	8.38	8.34	8.30

extensive (near)-degeneracies. All the excited states from Figure 1 can be classified as belonging to the several different manifolds: Rydberg, valence $n \rightarrow \pi^*$, and valence $\pi \rightarrow \pi^*$, as described in [17].

All the relevant valence MOs of Tz are degenerate at D_{3h}: the HOMO (π, e'') and closely lying HOMO-1 (n, e') pairs, as well as the Rydberg LUMO+1 (R_p, e'') and LUMO+2 (π^*, e'') pairs. The only low-lying non-degenerate orbital is the s-like Rydberg LUMO (R_s, a_1').

Owing to this degeneracy pattern, all the states from Figure 1 are derived from the transitions involving degenerate MOs, and, consequently, many of them are subject to JT distortions, as evidenced by the splittings between the degenerate states at the cation (C_{2v}) geometry (right panel of Figure 1).

The $\pi \rightarrow R_s$ and $n \rightarrow R_s$ Rydberg states form a familiar two-state JT manifold, and undergo distortions to lower-symmetry, pretty much like in the cation. One of the states relaxes to the minimum, and another—to the transition state along the pseudorotation coordinate. The symmetries of these $n \rightarrow R_s$ states are E': $e' \otimes a_1' \rightarrow E'$, where e' and a_1' are symmetries of n and R_s orbitals, respectively. The behaviour of the corresponding PES along a JT distortion coordinate is shown on the left panel of Figure 2. Note that the symmetry of the lowest adiabatic state changes along the pseudorotation coordinate, which gives rise to the geometric phase effect causing the breakdown of the Born–Oppenheimer approximation.

Excitations between the two doubly degenerate orbitals results in the four-state manifolds, two states being exactly degenerate as follows from the symmetry considerations. For example, symmetries of the electronic states in the $n \rightarrow \pi^*$ manifold can be obtained according to the irreducible representation multiplication rules: $e' \otimes e'' \rightarrow A_1'' + A_2'' + E''$, where e' and e'' are the symmetry of the n and π orbitals, respectively. Relative ordering of the states in these manifolds can be different, and three possible cases are shown in Figures 2(b)–(d). The distinctive feature of the four-state manifolds is that all four states are strongly coupled together. As shown both formally and numerically for the N_3^+ example [19,20], the result of these interactions is that the linear JT terms in the degenerate PESs in these manifolds almost vanish at the high symmetry geometry, and, consequently, the magnitude of the JT distortion is very small (e.g. 0.001 Å and 10^{-4} eV

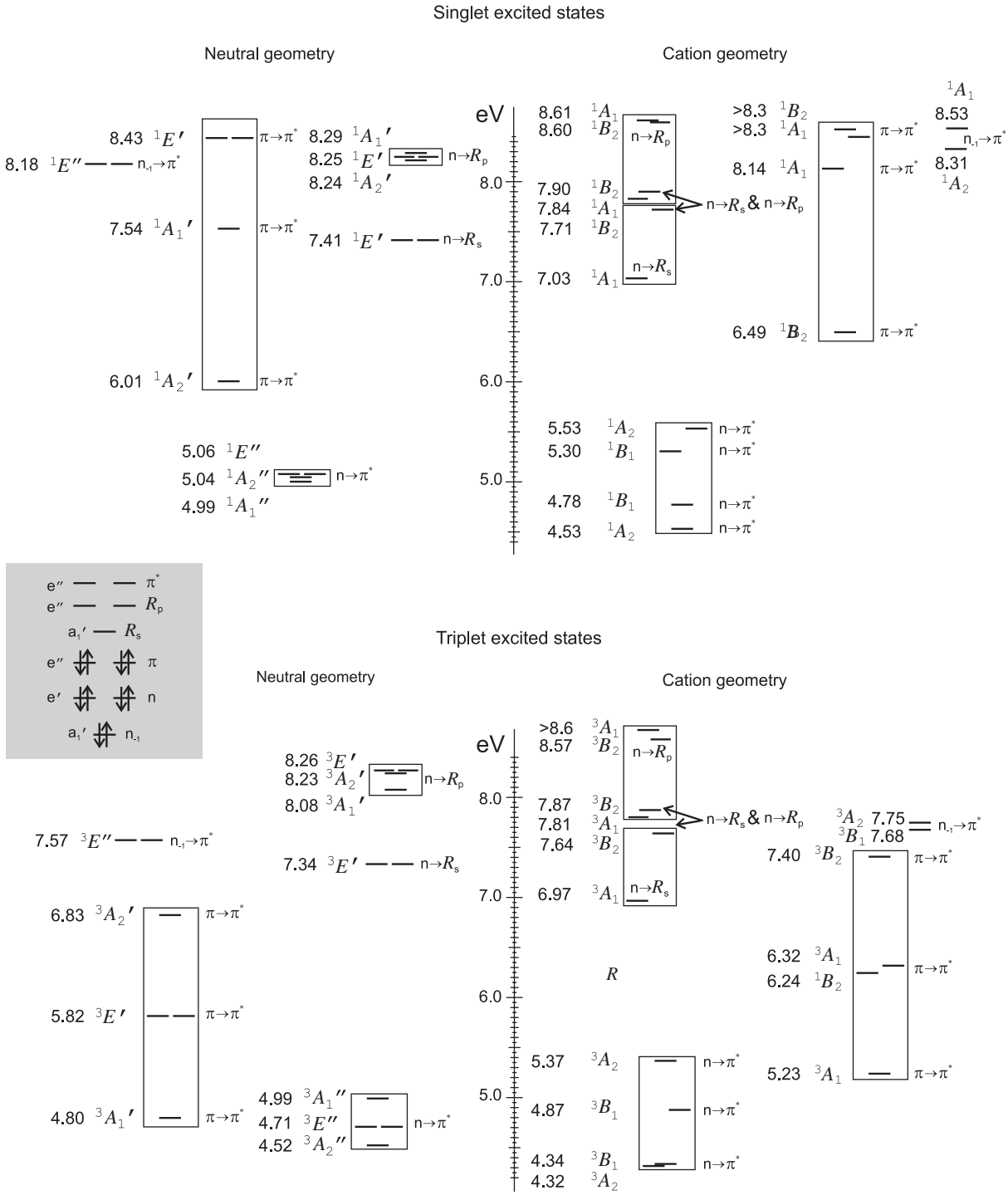

Figure 1. Singlet and triplet excited states at the neutral D_{3h} (left panel) and the distorted cation $^2A_1C_{2v}$ (right panel) geometries. The frontier MO ordering and the electronic configuration of the ground electronic state are shown in the insert. π and π* orbitals are similar to those of benzene, whereas orbitals denoted by *n* are derived from the nitrogens' lone pairs. R_s and R_p denote Rydberg orbitals of 3*s* and 3*p* character, respectively.

in N_3^+). Thus, all four surfaces have extrema either at or very close to the symmetric geometry, and the intersection appears to be glancing rather than conical, resembling avoided crossing in diatomics. Consequently, the symmetries of all four adiabatic PESs do not change as one moves around a D_{3h} point, provided that the radius of the rotation is greater than their minute JT distortions. Thus, one

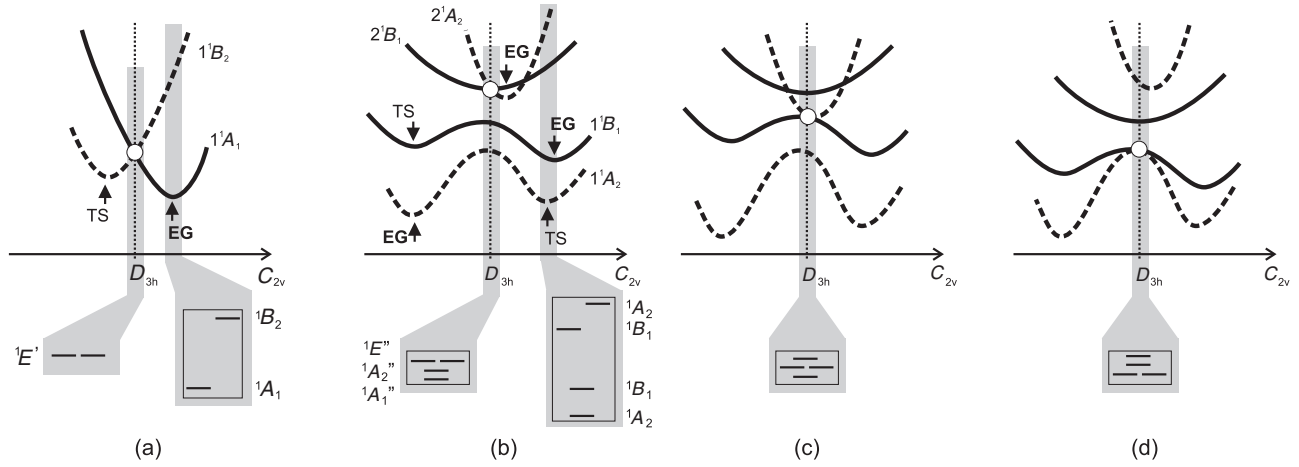

Figure 2. The cartoon illustrating the behaviour of PESs along Jahn–Teller displacements for the conical (a) and glancing-like (b)–(d) intersections (three different types of four-state manifolds are shown). Solid and dashed lines represent states of different symmetry. Symmetry labels in (a) are for the $n \rightarrow R_p$ conical intersection, and in (b) for the glancing intersection of four $n \rightarrow \pi^*$ states. Equilibrium geometries (EG) and transition states (TS) with respect to a pseudorotation coordinate (rotation around D_{3h} vertical axis) are also shown. See Appendix 1 for a detailed analysis of the four-state manifolds.

can safely employ adiabatic PESs for calculating vibrational wave functions.

The analysis of the three different degeneracy patterns in the four-state manifolds presented in Appendix 1 reveals that the two upper surfaces always have symmetric minima, as depicted in Figures 2(b)–(d). Thus, just from a degeneracy pattern at a symmetric configuration, the overall topology of the intersection can be mapped out. Note that without this analysis additional single-point calculation at a lower symmetry geometry (as in the right panel of Figure 1), or even at optimised equilibrium geometry of a distorted state, is not very informative, e.g. the conical and glancing degeneracies split in a similar way, whereas the PES topologies are rather different.

4. Optimised equilibrium geometries of the excited states in conical and glancing-like manifolds

In this section, we present and discuss equilibrium geometries of the states from the valence $n \rightarrow \pi^*$ and $n \rightarrow R_s$ manifolds. The latter structures are very similar to that of the cation, whose ground state is derived by ionisation from the n orbital. These manifolds give rise to the two dissociation channels of Tz initiated by the charge exchange between Cs and Tz^+, and represent two different types of the JT intersections: four-state glancing like and two-state conical ones. Optimised geometries and relaxation energies are summarised in Table 2. The definitions of geometrical parameters (angles and distances) are presented in Figure 3(c). Cartesian coordinates of optimised geometries are given in the Supplementary Materials which is available via the multimedia link on the online article webpage [35].

The Tz cation exhibits relatively strong JT distortions from D_{3h} geometry, which results in 0.47 eV energy gain, a difference between vertical and adiabatic ionisation energies of Tz. The potential energy profile along pseudorotation around the conical intersection is almost barrierless, as the transition state ($^2B_2$) is only about 0.01 eV higher than the ground $^2A_1$ state at the EOM-IP-CCSD/6-311++G** level of theory. These values can be compared to JT distortions in the benzene cation, whose ground state is derived from ionisation from the degenerate π-orbitals: relaxation of the cation from D_{6h} to D_{2h} is 0.18 eV with a transition state barrier for the pseudorotation only 0.003 eV above the ground state [30]. We attribute this difference to a stronger perturbation of the σ system by ionisation from the n orbitals.

The barrier for pseudo-rotation is below ZPE, and, therefore, the lowest vibrational wavefunctions of the cation are delocalised around the conical intersection. Note that proper account of the geometric phase effect is crucial for obtaining even qualitatively correct vibrational states [36,37]. The complications due to geometric phase can be avoided entirely by switching to diabatic representation, see, for example, [38] and references therein.

Although the glancing-like manifold of the four $n \rightarrow \pi^*$ states has more complicated electronic structure, the vibrational wave functions of the top two states can be computed within the BO approximation,

Table 2. Geometrical parameters of the ground electronic state of Tz, the Tz^+ cation, the $n \rightarrow \pi^*$ and $n \rightarrow R_s$ singlet excited states optimised equilibrium structures. Bond lengths are given in Angstroms, and angles are in degrees. The relaxation energies are calculated relative to the energy of the ground electronic state geometry.

	Ground electronic state			Singlet $n \rightarrow \pi^*$ excited states				$n \rightarrow R_s$		Cation	
	CCSD 6-311++G**	CCSD cc-pVTZ	Exp. [1]	EOM-CCSD 6-311++G**				EOM-CCSD 6-311++G**		EOM-IP-CCSD 6-311++G**	
	$^1A_1$ D_{3h}	$^1A_1$ D_{3h}	D_{3h}	1^1A_2 C_{2v}	1^1B_1 C_{2v}	2^1B_1 C_{2v}	2^1A_2 D_{3h}	$^1A_1$ C_{2v}	$^1B_2$ C_{2v}	$^2A_1$ C_{2v}	$^2B_2$ C_{2v}
ΔE, eV	–	–	–	−1.01	−1.00	−0.68	−0.36	−0.42	−0.43	−0.47	−0.45
CN_1	1.336	1.327	1.338	1.380	1.367	1.336	1.347	1.332	1.325	1.324	1.327
CN_2	1.336	1.327	1.338	1.299	1.304	1.348	1.347	1.336	1.324	1.334	1.330
CN_3	1.336	1.327	1.338	1.364	1.373	1.358	1.347	1.319	1.336	1.324	1.336
CH_1	1.087	1.077	1.084	1.074	1.081	1.084	1.083	1.089	1.084	1.090	1.084
CH_2	1.087	1.077	1.084	1.089	1.083	1.081	1.083	1.085	1.088	1.086	1.088
CNC_1	113.95	114.02	113.2	124.55	117.94	119.33	118.87	115.66	123.93	116.42	123.93
NCN_1	126.05	125.98	126.8	109.39	124.30	121.39	121.12	127.50	112.96	126.64	112.56
NCN_2	126.05	125.98	126.8	126.30	118.08	120.35	121.12	116.93	124.06	116.70	123.53
NCH_1	116.97	117.01	116.6	125.30	117.85	119.30	119.43	116.25	123.52	116.68	123.67
NCH_2	116.97	117.01	116.6	116.55	122.64	119.87	119.43	122.49	116.88	122.16	117.32

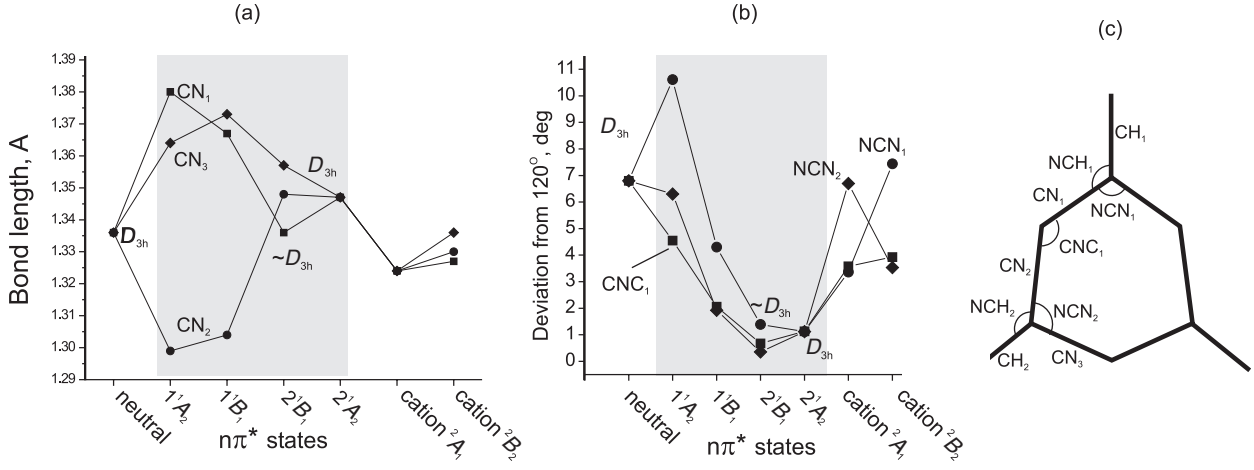

Figure 3. CN bond lengths (a) and deviations from 120° of hexagon ring angles (i.e. 120-NCN_1, 120-NCN_2, and 120-CNC) for the neutral Tz, the cation, and the $\pi^* \longleftarrow n$ excited states. The definitions of structural parameters are shown in (c). The neutral and the top $\pi^* \longleftarrow n$ states are of D_{3h} symmetry, and the 2^1B_1 state is nearly D_{3h} symmetric.

due to special features of the four-state manifolds, which are explained in the Appendix. Note that the displacements from D_{3h} symmetry are indeed minute, as evidenced by the data in Table 2 and Figure 3.

Figure 3 allows one to quantify the magnitude of JT displacements in terms of bond-lengths and angles. Tz has D_{3h} symmetry if the three CN bonds are of equal length, and the sum of CNC and NCN angles is 240°, that is, if CNC and NCN deviate from 120° to an equal extent but with the opposing sign. Figure 3 shows that this is exactly the case for the top 2^1A_2 state from the $n \rightarrow \pi^*$ manifold. The 2^1B_1 state is also almost symmetric, as it is expected for the glancing-like manifold. The two lowest states from this manifold (1^1A_2 and 1^1B_1) are significantly distorted to C_{2v} geometry, as the corresponding PESs have a maximum at D_{3h}. Note that the relaxation energies (difference between the Tz ground state geometry and the excited-state optimised structures) from Table 2 are similar in magnitude for all states (0.4–1.0 eV), however, for the two top states the relaxation occurs along the D_{3h} 'seam' of glancing-like intersection, whereas the two lowest states relax along the JT coordinate to C_{2v}.

Note that equilibrium geometries of the Rydberg $n \rightarrow \pi^*$ states are indeed very close to those of the cation: the differences are less than 0.008 A for the CN

Table 3. Harmonic frequencies (cm^{-1}) and infrared intensities ($km\,mol^{-1}$, in parenthesis) of the $n \rightarrow \pi^*$ excited states and the cation. The displacements from the neutral ground-state geometry along normal modes ($\text{Å}\ amu^{-1/2}$) are also shown whenever greater than $0.01\ \text{Å}\ amu^{-1/2}$. In plane and out of plane vibrations are labelled with (p) and (o), respectively.

			Frequencies		Displacement from GS equilibrium geometry					
					Singlet n/π^* excited states				Cation	
Normal modes			6-311++G**	Exp. [1]	1^1A_2	1^1B_1	2^1B_1	2^1A_2	$^2A_1$	$^2B_2$
1	$2E''$	Ring(o)	350.09 (0.0)	340						
2	$2E''$	Ring(o)	350.09 (0.0)	340						
3	$5E'$	Ring(p)	697.60 (14.1)	675	−11.09	0.41	−0.01		−1.58	1.26
4	$5E'$	Ring(p)	697.60 (14.1)	675	0.55	−0.02			6.92	6.97
5	$2a_2''$	Ring(o)	741.81 (33.2)	737						
6	$^1A_2''$	CH(o)	935.20 (0.0)	925						
7	$1E''$	CH(o)	1004.63 (0.9)	≈1031						
8	$1E''$	CH(o)	1004.63 (0.9)	≈1031						
9	$3a_1'$	Ring(p)	1030.03 (8.5)	992	9.64	0.13	0.11	0.10	7.34	9.93
10	$2a_2'$	Ring(p)	1110.48 (0.0)	≈1251					−11.09	−11.15
11	$2a_1'$	Ring(p)	1164.23 (0.0)	1132	−7.07	0.35	0.32	0.30	−6.55	−5.82
12	$4E'$	CH(p)	1217.74 (0.5)	1174	3.66	−0.07	−0.06		1.75	3.83
13	$4E'$	CH(p)	1217.74 (0.5)	1174	−0.12				2.58	3.23
14	$2a_2'$	CH(p)	1420.76 (0.0)	≈1617					1.43	0.90
15	$3E'$	Ring(p)	1464.63 (64.3)	1410	−3.78	0.05	−0.03		2.24	2.43
16	$3E'$	Ring(p)	1464.63 (64.3)	1410	−0.32				−2.17	−2.07
17	$2E'$	Ring(p)	1644.42 (135.3)	≈1556	−2.26	0.12			3.96	2.91
18	$2E'$	Ring(p)	1644.42 (135.3)	≈1556	−0.93	0.05			1.79	1.39
19	$1E'$	CH(p)	3217.98 (17.3)	3056	0.33				−0.40	−0.79
20	$1E'$	CH(p)	3217.98 (17.3)	3056	1.23				−1.54	−1.78
21	$^1A_1'$	CH(p)	3221.92 (0.0)	≈3042	−1.69	−0.02	−0.01	−0.01	−2.70	−2.46

bonds and less than 0.8° for the angles. Likewise, the energy gain upon the JT relaxation is also very similar (within 1 kcal mol^{-1}).

Finally, the magnitude of geometric relaxation can be analysed in terms of the displacements along the normal modes of the neutral Tz, as presented in Table 3. The units for normal coordinates, which are the eigenstates of the mass-weighted Hessian, are $\text{Å}\ amu^{-1/2}$. The two nearly symmetric $n \rightarrow \pi^*$ states are distorted mostly along the three fully symmetric a_1' normal modes, the two other states and the cation are distorted along the in-plane normal modes of lower symmetries. The two lowest $n \rightarrow \pi^*$ states, 1^1A_2 and 1^1B_1, are asymmetric and the most active non-symmetric normal mode for both states is $5e'$, with −11.07 and 0.34 displacements, respectively. This mode corresponds to the JT coordinate of the $n \rightarrow \pi^*$ states. Coupling between the normal modes is considerable at larger geometry relaxations, and several other non-a_1' modes are active in the 1^1A_2 state.

Normal mode mixing is even stronger in the cation (and the $n \rightarrow R_s$ excited state) due to larger distortion relative to the neutral D_{3h} equilibrium geometry. Nevertheless, only two non-a_1' normal modes contribute considerably: $5e'$ and $2a_2'$ with 6.92 and −11.09 displacements, respectively, which are the most active normal modes. The JT coordinate is $5e'$ with opposite displacements of −1.58 and 1.26 for $^2A_1$ ground and $^2B_2$ transition states of the cation, respectively.

In the recent study [16–18], it has been concluded that Tz dissociates symmetrically when prepared in the $n \rightarrow \pi^*$ state, and follows asymmetric dissociation from the Rydberg $n \rightarrow R_s$ excited state. Displacements along the normal modes of the neutral Tz molecule from the neutral equilibrium geometry shown in Table 3 demonstrate the suggested mechanisms. Indeed, the symmetric excited state, whose structure is different from the D_{3h} ground state only by displacements along a_1' normal modes (2^1A_2), will acquire symmetric (a_1') vibration quanta upon the relaxation to the ground state, and in the case of fast, ballistic, dissociation to the three HCN, this vibrational excitation will transform into symmetrically distributed momenta of the fragments. Vibrational excitation of the non-a_1' normal modes acquired via the Rydberg state will lead to the asymmetric momentum partitioning.

5. Conclusions

We characterised electronically excited states of Tz at the equilibrium ground state geometry and at the geometry of the cation. Moreover, full geometry optimisations of the selected excited states were performed. JT distortions in the cation and the excited states were analysed both formally and numerically. Analysis of the electronic structure of the excited states allows one to predict symmetry of the equilibrium geometry of the states derived from excitations between the two pairs of doubly degenerate orbitals from a single-point calculation at a symmetric geometry. This was demonstrated by discussing possible PES topologies and symmetries of the states from the two- and four-manifolds giving rise to the conical and glancing intersections, respectively. Formal conclusions are supported by the optimised equilibrium geometries of the selected excited states.

This analysis can be applied to predict symmetries of the equilibrium structures of the states from four-state manifolds in other benzene-like aromatic molecules, whose electronic structure is similar to that of Tz.

Recently, we suggested [16,17] that these two different types of manifolds give rise to two different dissociation mechanisms, concerted and stepwise. The difference between the two manifolds would also manifest itself in the vibrational spectra of the respective excited states. The order of vibrational states for the electronic state with the conical intersection should be affected by the geometric phase effect as it was observed in Na_3 [39,40] and theoretically documented in N_3 [36,37] however, we expect no signature of the geometric phase effect in the case of the glancing-like intersections.

Acknowledgements

AIK acknowledges support from the National Science Foundation (CHE-0616271). This work is conducted under the auspices of the iOpenShell Center for Computational Studies of Electronic Structure and Spectroscopy of Open-Shell and Electronically Excited Species supported by the National Science Foundation through the CRIF:CRF CHE-0625419+0624602+0625237 grant. AIK is grateful to the Institute of Mathematics and its Applications in Minnesota for its hospitality and productive environment during her stay at IMA as a visiting professor.

References

[1] K.K. Innes, I.G. Ross, and W.R. Moomaw, J. Molec. Spect. **132**, 492 (1988).
[2] G.S. Ondrey and R. Bersohn, J. Chem. Phys. **81**, 4517 (1984).
[3] J.D. Webb, K.M. Swift, and E.R. Bernstein, J. Chem. Phys. **73**, 4891 (1980).
[4] S.R. Goates, J.O. Chu, and G.W. Flynn, J. Chem. Phys. **81**, 4521 (1984).
[5] I.C. Walker, M.H. Palmer, and C.C. Ballard, Chem. Phys. **167**, 61 (1992).
[6] S.V. Pai, C.F. Chabalowski, and B.M. Rice, J. Phys. Chem. **100**, 5681 (1996).
[7] T. Gejo, J.A. Harrison, and J.R. Huber, J. Chem. Phys. **100**, 13941 (1996).
[8] J.E. DelBene, J.D. Watts, and R.J. Bartlett, J. Chem. Phys. **106**, 6051 (1997).
[9] K.Y. Song and M.A. Collins, Chem. Phys. Lett. **335**, 481 (2001).
[10] J.M. Oliva, E.M.DG Azenha, H.D. Burrows, R. Coimbra, J.S.S de Melo, M.L. Canle, M.I. Fernandez, J.A. Santaballa, and L. Serrano-Andres, Chem. Phys. Chem. **6**, 306 (2005).
[11] Y.A. Dyakov, A.M. Mebel, S.H. Lin, Y.T. Lee, and C.K. Ni, J. Phys. Chem. A **111**, 9591 (2007).
[12] A. Devarajan, A.V. Gaenko, Y.G. Khait, and M.R. Hoffmann, J. Phys. Chem. A **112**, 2677 (2008).
[13] Y. Osamura, M. Unno, and K. Hashimoto, J. Am. Chem. Soc. **109**, 1370 (1987).
[14] J.H. Kim and H.L. Kim, Chem. Phys. Lett. **333**, 45 (2001).
[15] J. Lee, E.J. Dong, D.S. Jin, K.Y. Song, and M.A. Collins, Phys. Chem. Chem. Phys. **6**, 945 (2004).
[16] J.D. Savee, V.A. Mozhayskiy, J.E. Mann, A.I. Krylov, and R.E. Continetti, Science **321**, 826 (2008).
[17] V.A. Mozhayskiy, J.D. Savee, J.E. Mann, R.E. Continetti, and A.I. Krylov, J. Phys. Chem. A **112**, 12345 (2008).
[18] J.D. Savee, J.E. Mann, and R.E. Continetti, J. Phys. Chem. A, (2009) submitted.
[19] V.A. Mozhayskiy, D. Babikov, and A.I. Krylov, J. Chem. Phys. **124**, 224309 (2006).
[20] J.J. Dillon and D.R. Yarkony, J. Chem. Phys. **126**, 124113 (2007).
[21] G.D. Purvis and R.J. Bartlett, J. Chem. Phys **76**, 1910 (1982).
[22] T.H. Dunning, J. Chem. Phys. **90**, 1007 (1989).
[23] H. Sekino and R.J. Bartlett, Int. J. Quant. Chem. Symp. **26**, 255 (1984).
[24] H. Koch, H.J.Aa Jensen, P. Jrgensen, and T. Helgaker, J. Chem. Phys. **93**, 3345 (1990).
[25] J.F. Stanton and R.J. Bartlett, J. Chem. Phys. **98**, 7029 (1993).
[26] S.V. Levchenko and A.I. Krylov, J. Chem. Phys. **120**, 175 (2004).
[27] A.I. Krylov, Annu. Rev. Phys. Chem. **59**, 433 (2008).
[28] D. Sinha, D. Mukhopadhyay, and D. Mukherjee, Chem. Phys. Lett. **129**, 369 (1986).
[29] J.F. Stanton and J. Gauss, J. Chem. Phys. **101**, 8938 (1994).
[30] P.A. Pieniazek, S.E. Bradforth, and A.I. Krylov, J. Chem. Phys. **129**, 074104 (2008).

[31] S.V. Levchenko, T. Wang, and A.I. Krylov, J. Chem. Phys. **122**, 224106 (2005).
[32] Y. Shao, L.F. Molnar, Y. Jung, J. Kussmann, C. Ochsenfeld, S. Brown, A.T.B Gilbert, L.V. Slipchenko, S.V. Levchenko, D.P. O'Neil, R.A. Distasio Jr, R.C. Lochan, T. Wang, G.J.O Beran, N.A. Besley, J.M. Herbert, C.Y. Lin, T. Van Voorhis, S.H. Chien, A. Sodt, R.P. Steele, V.A. Ras-solov, P. Maslen, P.P. Korambath, R.D. Adamson, B. Austin, J. Baker, E.F.C Bird, H. Daschel, R.J. Doerksen, A. Drew, B.D. Dunietz, A.D. Dutoi, T.R. Furlani, S.R. Gwaltney, A. Heyden, S. Hirata, C.-P. Hsu, G.S. Kedziora, R.Z. Khalliulin, P. Klunziger, A.M. Lee, W.Z. Liang, I. Lotan, N. Nair, B. Peters, E.I. Proynov, P.A. Pieniazek, Y.M. Rhee, J. Ritchie, E. Rosta, C.D. Sherrill, A.C. Simmonett, J.E. Subotnik, H.L. Woodcock III, W. Zhang, A.T. Bell, A.K. Chakraborty, D.M. Chipman, F.J. Keil, A. Warshel, W.J. Herhe, H.F. Schaefer III, J. Kong, A.I. Krylov, P.M.W Gill, and M. Head-Gordon, Phys. Chem. Chem. Phys. **8**, 3172 (2006).
[33] W.J. Hehre, R. Ditchfield, and J.A. Pople, J. Chem. Phys. **56**, 2257 (1972).
[34] R. Krishnan, J.S. Binkley, R. Seeger, and J.A. Pople, J. Chem. Phys. **72**, 650 (1980).
[35] See supplementary materials for the molecular structures and total energies.
[36] D. Babikov, B.K. Kendrick, P. Zhang, and K. Morokuma, J. Chem. Phys. **122**, 044315 (2005).
[37] D. Babikov, V.A. Mozhayskiy, and A.I. Krylov, J. Chem. Phys. **125**, 084306 (2006).
[38] H. Koppel, W. Domcke, and L.S. Cederbaum, *The Multi-mode Vibronic-coupling Approach* (World Scientific, Singapore, 2004), pp. 323–367, Chap. 7.
[39] G. Delacretaz, E.R. Grant, R.L. Whetten, L. Woste, and J.W. Zwanziger, Phys. Rev. Lett. **56**, 2598 (1986).
[40] B. Kendrick, Phys. Rev. Lett. **79**, 2431 (1997).
[41] V.I. Pupsyshev (private communication).
[42] W.D. Hobey and A.D. McLachlan, J. Chem. Phys. **33**, 1695 (1960).
[43] W. Moffitt and A.D. Liehr, Phys. Rev. **106**, 1195 (1957).

Appendix 1. Four-state glancing intersections

This appendix describes the electronic structure of the four-state glancing intersections (GIs) derived from the excitations between two degenerate pairs of MOs [19,20,41]. Below we explain why the degenerate states in these intersections exhibit negligible JT distortions [41] and demonstrate that the three PES patterns shown in Figure 2 represent all possible topographies of the four-state manifolds.

In a D_{3h} molecule, the degenerate MOs are of e' or e'' symmetry. In C_{2v} (the highest symmetry in which the degeneracy is lifted), these degenerate orbitals become A_1+B_2 and A_2+B_1, respectively.

Consider excitations from the fully occupied doubly degenerate (e_A^{occ} and e_B^{occ}) MOs to the two degenerate virtual orbitals (e_A^{virt} and e_B^{virt}). Primes and subindices are omitted for the rest of this section for the sake of generality. Once spin and spatial symmetry is properly accounted for, these transitions give rise to the four electronic configurations [19] (Configuration State Functions, CSFs):

$$\begin{aligned} \alpha_A &: e_B^{\mathrm{occ}} \rightarrow e_B^{\mathrm{virt}}, \\ \beta_B &: e_A^{\mathrm{occ}} \rightarrow e_B^{\mathrm{virt}}, \\ \gamma_B &: e_B^{\mathrm{occ}} \rightarrow e_A^{\mathrm{virt}}, \\ \delta_A &: e_A^{\mathrm{occ}} \rightarrow e_A^{\mathrm{virt}}. \end{aligned} \tag{A1}$$

The CSFs of the same symmetry can mix, and at D_{3h} they mix with equal coefficients due to the exact electronic degeneracy of the MOs. Thus, the wave functions of the four excited states are: $\alpha_A \pm \delta_A$ and $\beta_B \pm \gamma_B$ (omitting the normalisation coefficients). Only two out of these four states are exactly degenerate, i.e. $e \otimes e \rightarrow E + A + B$ (this is valid for any combination of primes in the MOs symmetry labels).

Let us first consider the topography of the two degenerate states. Assume that these two electronic states are $\alpha_A - \delta_A$ and $\beta_B + \gamma_B$, as in the cyclic N_3 cation [19]. An elegant transformation of the MOs to the complex-valued form proposed by Pupyshev [41] significantly simplifies further derivations:

$$\begin{aligned} e_{\pm}^{\mathrm{occ}} &= (e_A^{\mathrm{occ}} \pm i \cdot e_B^{\mathrm{occ}}) \\ e_{\pm}^{\mathrm{virt}} &= -(e_A^{\mathrm{virt}} \pm i \cdot e_B^{\mathrm{virt}}). \end{aligned} \tag{A2}$$

In these complex-valued MOs, the wave functions of the degenerate states assume the following form:

$$E_{\pm} = (\alpha_A - \delta_A) \pm i \cdot (\beta_B + \gamma_B), \tag{A3}$$

where $E_{\pm}$ excited states are the single excitations in the complex MO representation:

$$E_{\pm} : e_{\pm}^{\mathrm{occ}} \rightarrow e_{\pm}^{\mathrm{virt}}. \tag{A4}$$

For example, E_+ can be written in a shorthand notation as:

$$\begin{aligned} E_+ &= [(e_B^{\mathrm{occ}} \rightarrow e_B^{\mathrm{virt}}) - (e_A^{\mathrm{occ}} \rightarrow e_A^{\mathrm{virt}})] + i \cdot [(e_A^{\mathrm{occ}} \rightarrow e_B^{\mathrm{virt}}) \\ &\quad + (e_B^{\mathrm{occ}} \rightarrow e_A^{\mathrm{virt}})] \\ &= (e_A^{\mathrm{occ}} + i \cdot e_B^{\mathrm{occ}}) \rightarrow (-e_A^{\mathrm{virt}} - i \cdot e_B^{\mathrm{virt}}) \\ &= e_+^{\mathrm{occ}} \rightarrow e_+^{\mathrm{virt}}, \end{aligned} \tag{A5}$$

where $e_x^{\mathrm{occ}} \rightarrow e_y^{\mathrm{virt}}$ denotes a determinant in which an electron is excited from the e_x^{occ} to e_y^{virt} orbital.

Once the wave functions of the degenerate electronic states are written in the complex MO representation (A4), it is obvious that the two states are doubly excited with respect to each other. Thus, the matrix element of a one-electron operator (e.g. nuclear derivative) between these two states is exactly zero, suggesting zero gradient along a JT distortion. This propriety of doubly degenerate states has been noted before, for example, in the studies of the benzene excited states [42,43].

Below we show that the linear term in the potential energy almost vanishes along any coordinate that lifts the

degeneracy in GI, or that the first derivative of the electronic state's energy is zero along such a coordinate. Neglecting non-Hellmann–Feynman terms, we consider the matrix elements of the derivative of an electronic Hamiltonian along some coordinate Q, $\partial H/\partial Q$:

$$\begin{bmatrix} \langle \Psi_{E_+} | \dfrac{\partial H}{\partial Q} | \Psi_{E_+} \rangle \langle \Psi_{E_+} | \dfrac{\partial H}{\partial Q} | \Psi_{E_-} \rangle \\ \langle \Psi_{E_-} | \dfrac{\partial H}{\partial Q} | \Psi_{E_+} \rangle \langle \Psi_{E_-} | \dfrac{\partial H}{\partial Q} | \Psi_{E_-} \rangle \end{bmatrix}. \tag{A6}$$

The diagonal matrix elements are equal since E_+ and E_- are the complex-conjugates of each other by construction (A3). Moreover, since the diagonal matrix elements $\langle \Psi_{E_\pm} | (\partial H/\partial Q) | \Psi_{E_\pm} \rangle$ are always fully symmetric, they can be non-zero only for the Hamiltonian derivatives along a fully symmetric coordinate. Thus, the gradients of both degenerate surfaces along a fully symmetric coordinate are equal and may be non-zero, which means any fully symmetric coordinate is a seam of the intersection. Diagonal elements are exactly zero for the derivative taken along any non-fully symmetric coordinate, i.e. along any coordinate that lifts the degeneracy (a JT distortion). If the derivative of the Hamiltonian, and therefore the derivative of the energy, along the JT coordinate is zero, then the potential energy function has an extremum at the symmetric D_{3h} geometry.

The coupling element is exactly zero only within the 4-electron-in-2-orbital model and for one-electron Hamiltonians. The presence of other electronic configurations in correlated wave functions can, in principle, result in non-zero couplings. However, as demonstrated by highly accurate multi-reference CI calculations of N_3^+ [20] (and confirmed by the EOM-CC calculations in the present work), the resulting JT distortions are extremely small.

To conclude, the linear term along JT distortion coordinates is (almost) zero and the extrema of both surfaces are very close to D_{3h}. One can easily determine whether these two intersecting surfaces have minima, maxima or both near the intersection, if one considers two other non-degenerate states from the $e \otimes e$ manifold. As shown at the bottom of Figure 2, there are only three possible relative orderings of two degenerate and two non-degenerate states: the degenerate states are the the highest (b), the lowest (d), or in between the two non-degenerate states (c). Solid and dashed lines in Figure 2 denote the electronic states of different symmetry. As described in [19], each two states of the same symmetry (one non-degenerate and another one from the degenerate pair) due to the symmetry allowed coupling exhibit an avoided-crossing like behaviour, as shown in Figure 2(b–d). At a few points along the GI seam where an accidental degeneracy of three states occurs, the conical like intersection will be present between two surfaces of the same symmetry.